

Turbulence and secondary motions in square duct flow

SERGIO PIROZZOLI¹, DAVIDE MODESTI²,
PAOLO ORLANDI¹ AND FRANCESCO GRASSO²

¹Dipartimento di Ingegneria Meccanica e Aerospaziale, Sapienza Università di Roma
Via Eudossiana 18, 00184 Roma, Italy

²Cnam-Laboratoire DynFluid, 151 Boulevard de L'Hopital, 75013 Paris

(Received 18 February 2022)

We study turbulent flows in pressure-driven ducts with square cross-section through direct numerical simulation in a wide enough range of Reynolds number to reach flow conditions which are representative of fully developed turbulence. Numerical simulations are carried out over extremely long integration times to get adequate convergence of the flow statistics, and specifically high-fidelity representation of the secondary motions which arise. The intensity of the latter is found to be in the order of 1-2% of the bulk velocity, and unaffected by Reynolds number variations. The smallness of the mean convection terms in the streamwise vorticity equation points to a simple characterization of the secondary flows, which in the asymptotic high- Re regime are found to be approximated with good accuracy by eigenfunctions of the Laplace operator. Despite their effect of redistributing the wall shear stress along the duct perimeter, we find that secondary motions do not have large influence on the mean velocity field, which can be characterized with good accuracy as that resulting from the concurrent effect of four independent flat walls, each controlling a quarter of the flow domain. As a consequence, we find that parametrizations based on the hydraulic diameter concept, and modifications thereof, are successful in predicting the duct friction coefficient.

1. Introduction

Internal flows within straight ducts having non-circular cross-section are common in many engineering applications, such as water draining or ventilation systems, nuclear reactors, heat exchangers and turbomachinery. Within this class of flows, square ducts have attracted most of the interest, and these are the subject of this study. Pioneering studies of flows in duct with complex cross-sections are due to Prandtl (1927); Nikuradse (1930), who first highlighted the presence of secondary motions in the cross-stream plane, hence explaining the typical bending of the mean streamwise velocity iso-lines towards the duct corners. Although the intensity of the secondary flow is a small fraction of the main stream (typically, a few percent), it may have some important practical impact, having the general role of redistributing friction and heat flux along the duct perimeter (Leutheusser 1963). In open-channel flows, secondary motions move fluid with relatively low streamwise momentum towards the centre portion of the channel, hence causing a depression of the velocity maximum below the free surface (Nezu 2005). Furthermore, secondary motions play a major role in processes of sediment transport and river bed erosion (Adrian & Marusic 2012). Hence, it is clear that robust physical insight

and accurate prediction of flows inside channels with complex shape is of utmost interest in the engineering practice.

Secondary flows are obviously associated with the presence of non-zero streamwise vorticity (Bradshaw 1987) which in turn may arise because of skewing of existing spanwise vorticity as in the case of duct bends (hence giving rise to Prandtl's secondary motions of the first kind), and/or because of Reynolds stress gradients in the presence of non-circular cross-section (secondary motions of the second kind), which is the case of the present paper. Secondary motions in square ducts are known to come in the form of eight counter-rotating eddies bringing high-momentum fluid from the duct core towards the corners, and to have a typical intensity of about 1% the duct bulk velocity (Prandtl 1927). Modeling secondary flows is a challenging task for turbulence models, as it is well known that classical models based on the isotropic eddy viscosity ansatz cannot generate self-sustained secondary motions in straight ducts (Speziale 1982; Mani *et al.* 2013). Quantitative measurements of secondary motions in ducts date back to the studies of Hoagland (1960); Brundrett & Baines (1964); Gessner & Jones (1965), who first attempted to shed light on the mechanisms of vorticity generation and on the effect of Reynolds number variation. Whereas those studies agree that secondary motions are generated from gradients of the Reynolds stresses, Brundrett & Baines (1964) reported that convection of mean streamwise vorticity provides an important contribution to the overall vorticity balance, whereas Gessner & Jones (1965) reported convection to be at least one order of magnitude less than the other balance terms in the mean vorticity equation. Brundrett & Baines (1964) further argued that secondary eddies should not be affected by the Reynolds number, whereas Gessner & Jones (1965) found that their intensity as a fraction of the bulk duct velocity decreases with increasing Reynolds number. Consistent with the latter statement, Launder & Ying (1972) argued that the typical velocity scale of the secondary motions is the friction velocity, rather than the bulk velocity. In a paper devoted to developing RANS closures for turbulent flows in ducts with complex cross-section, Demuren & Rodi (1984) pointed out that the contrasting conclusions of experimental studies regarding the Reynolds number dependence of secondary flows are likely due to incomplete flow development and/or inaccuracy of measurements. From scrutiny of previous experimental data, those authors argued that the longitudinal vorticity equations is controlled by balance between the Reynolds stress gradients and convection from the secondary motions, and that the terms involving the difference of the normal stresses and of the secondary shear stress are comparable in magnitude.

Given the rather inconclusive outcome of experimental studies, it is clear that direct numerical simulation (DNS) may be a valuable tool to shed light on the nature of the secondary motions, as it allows to accurately evaluate all the quantities which may be responsible for their occurrence and sustainment, especially giving access to the near-wall region, frequently disregarded in experiments owing to insufficient spatial resolution. The first DNS of incompressible square duct flow was carried out by Gavrilakis (1992), at bulk Reynolds number $Re_b = 2hu_b/\nu = 4410$ (where h is the duct half side, u_b is the bulk velocity in the duct, and ν is the fluid kinematic viscosity), which corresponds to a friction Reynolds number $Re_\tau^* = hu_\tau^*/\nu = 150$, where $u_\tau^* = (\tau_w^*/\rho)^{1/2}$ is the mean friction velocity, and τ_w^* is the mean wall shear stress. Irrespective of the presence of secondary motions, the mean flow along the wall bisectors was found to be similar to the case of a plane channel. Contrary to the claims of Demuren & Rodi (1984), analysis of the mean streamwise vorticity equation showed that the gradients of the Reynolds stresses are approximately balanced by viscous diffusion, whereas convection is less important. This result was also confirmed by DNS at $Re_\tau^* \approx 300$ by Huser & Biringen (1993), although carried out with marginal spatial resolution. Uhlmann *et al.* (2007); Pinelli *et al.* (2010)

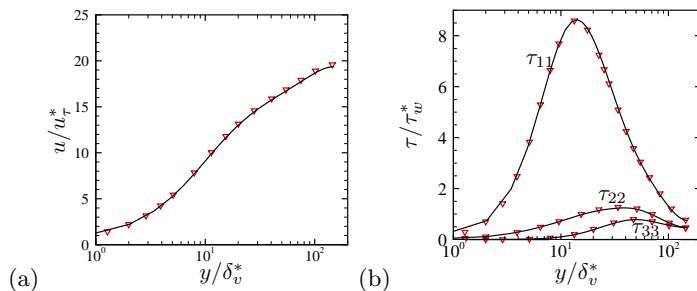


Figure 1: Profiles of mean velocity (a) and turbulent normal stresses (b) along wall bisector for flow case A (lines) compared with DNS data of Pinelli *et al.* (2010) (triangles).

first attempted to numerically span a range of (low) Reynolds numbers from $Re_\tau^* \approx 80$ to $Re_\tau^* \approx 225$, also noticing that much longer time integration intervals are necessary to achieve convergence of the flow statistics than done in earlier studies. Their study especially focused on establishing the spatial association between streamwise vorticity and streamfunction of the cross flow. Those authors noticed that as the Reynolds number increases the peak locations of ω_x and ψ start to be segregated, the former remaining approximately constant in wall units, and the latter in outer units. Vinuesa *et al.* (2014) carried out DNS of duct flow in square and rectangular channels at $Re_\tau^* = 180 - 300$, with special attention to establishing the effect of the channel aspect ratio. Inner scaling with the local wall friction was found to yield greater universality of the flow statistics as compared to scaling based on the mean wall friction. Zhang *et al.* (2015) carried out DNS of square duct flow up to $Re_\tau^* = 600$, the highest reached so far. They found that below $Re_\tau^* = 300$, low-Reynolds number effects are dominant, and observed a continuous trend in the position of the vortex centers, which move towards the wall bisectors as the Reynolds number increases. Although this was not commented in depth, their data seem to indicate growth of the intensity of the secondary motions with the Reynolds number, when expressed in bulk units. Marin *et al.* (2016) carried out DNS of hexagonal duct flow up to $Re_\tau^* \approx 400$ and compared the secondary motions with those observed in square duct flow, finding a similar trend with the Reynolds number as observed by Pinelli *et al.* (2010), namely that the streamfunction scales in outer units, whereas the streamwise vorticity scales in inner units.

In summary, although the flow in square ducts has been frequently studied both through experiments and DNS, and it is used as a prototype for the study of flows in ducts with complex cross-section, it appears that several fundamental questions have not been satisfactorily answered. The present paper then aims at elucidating the following issues: i) which is the correct velocity scale for the secondary motions?; ii) to what extent does the universal inner-layer law apply to the mean streamwise velocity profile?; iii) what is the nature of the secondary motions, and is it possible to provide an approximate characterization in the high-Reynolds-number limit?; iv) what is the effect of the secondary motions on the bulk flow features, namely the friction law? In order to answer these questions a novel DNS database has been developed covering Reynolds number up to $Re_\tau^* \approx 1000$, as described in the following section.

2. The numerical database

The numerical simulation of turbulent flow in square ducts in the incompressible limit is a much more challenging task for numerical algorithms than the canonical cases of plane

Case	Re_b	Re_τ^*	$C_f \times 10^{-3}$	N_x	N_y	N_z	Δx^*	Δz^*	Δy_w^*	$\Delta t_{av}^* u_\tau^*/h$	$\epsilon \times 10^{-4}$	$\epsilon_s \times 10^{-2}$
A	4410	151	9.38	512	128	128	5.5	3.1	0.71	2204	9.71	4.10
B	7000	225	8.34	640	144	144	6.7	5.1	0.82	1605	2.69	3.30
C	17800	516	6.76	1024	256	256	9.6	6.7	0.88	1385	3.31	2.30
D	40000	1048	5.53	2048	512	512	9.7	6.7	0.63	493	1.69	8.16

Table 1: Flow parameters for square duct DNS. Box dimensions are $6\pi h \times 2h \times 2h$ for all flow cases. $Re_b = 2hu_b/\nu$ is the bulk Reynolds number, and $Re_\tau^* = hu_\tau^*/\nu$ is the friction Reynolds number. Δx is the mesh spacing in the streamwise direction, and Δz , Δy_w are the maximum and minimum mesh spacings in the cross-stream direction, all given in global wall units, $\delta_v^* = \nu/u_\tau^*$. Δt_{av}^* is the effective averaging time interval, and the convergence indices ϵ and ϵ_s are defined in equations (2.1)-(2.2).

channel and pipe flow. The main reason resides in the availability of only one direction of space inhomogeneity, which prevents the use of efficient inversion procedures for Poisson equations based on double trigonometric expansions (Kim & Moin 1985; Orlandi 2012). Although this difficulty can be circumvented through the use of two-dimensional Poisson solvers based on cyclic reduction (Gavrilakis 1992), similar efficiency can also be achieved with compressible algorithms made to operate at low Mach number (Modesti & Pirozzoli 2016a), thus avoiding the solution of a discrete Poisson equation, however at the expense of stiffness in the allowed time step for explicit integration of acoustic waves. In the present work we use a fourth-order co-located finite-difference solver, previously used for DNS of compressible turbulence, also in the low-Mach-number regime (Pirozzoli & Bernardini 2013; Modesti & Pirozzoli 2016b). Here, the convective terms in the Navier-Stokes equations are preliminarily expanded to quasi-skew-symmetric form, in such a way to discretely preserve total kinetic energy from convection (Pirozzoli 2010). Semi-implicit time stepping is used for time advancement in order to relax the acoustic time step limitation, thus allowing efficient operation at low Mach number, also through the use of the entropy evolution equation rather than the total energy equation. The streamwise momentum equation is forced in such a way as to maintain a constant mass flow rate (the spatially uniform driving term is hereafter referred to as Π , see equation (4.1)), periodicity is exploited in the streamwise direction, and isothermal no-slip boundary conditions are used at the channel walls.

Let h be the duct half-side, the DNS have been carried out for a duct with $[-h : h] \times [-h : h]$ cross section, and whose length is $6\pi h$, the latter selected on the basis of preliminary box size sensitivity studies as well as conclusions of previous authors (Gavrilakis 1992). Four DNS have been carried out at bulk Mach number $M_b = u_b/c_w = 0.2$ (where c_w is the speed of sound at the wall temperature), and bulk Reynolds number $Re_b = 4000 - 40000$ (see table 1), and hereafter labeled with letters from A to D. The turbulence Mach number $M_t = u'/c_w$ nowhere exceeds 0.01 for any of the simulations, hence the present DNS may be regarded as representative of genuinely incompressible turbulence. For the sake of later reference, we will use the $+$ superscript to denote quantities made nondimensional with respect to the local wall friction, namely with $u_\tau = (\tau_w/\rho_w)^{1/2}$, $\delta_v = \nu/u_\tau$, and the $*$ superscript to denote quantities made nondi-

mensional with respect to the perimeter-averaged friction, $\tau_w^* = h\bar{\Pi}/2$, $u_\tau^* = (\tau_w^*/\rho_w)^{1/2}$, $\delta_v^* = \nu/u_\tau^*$.

In order to validate the numerical approach, flow case A is made to match the conditions of previous DNS studies (Gavrilakis 1992; Pinelli *et al.* 2010). A comparison with the latter dataset is shown figure 1, which supports excellent agreement of mean velocity and velocity fluctuation statistics. Statistical convergence of DNS is a crucial issue, and as pointed out by Oliver *et al.* (2014), the statistical error may be even dominant over the numerical error. In this respect, previous DNS of duct flow highlighted the need of extremely long averaging time intervals to achieve statistical convergence, typically several times longer than in plane channel flow. This issue is mainly associated with the weakness of secondary motions. Vinuesa *et al.* (2016) introduced a convergence indicator for duct flow based on use of the mean momentum balance equation (see equation (4.1)) similar to what is usually done for plane channel flow, in which linearity of the total stress is taken as an index of statistical convergence. Specifically, those authors considered the root-mean-square of the residual of equation (4.1) expressed in wall units (say R^*) and averaged over the wall bisector,

$$\epsilon = \left(\frac{1}{h} \int_0^h R^*(0, y)^2 dy \right)^{1/2}. \quad (2.1)$$

We have also considered an additional convergence indicator based on deviations of the computed statistical properties from the expected geometrical symmetry, which we define as

$$\epsilon_s = \frac{1}{u_b} \left[\frac{1}{4h^2} \int_{-h}^h \int_{-h}^h (\bar{u}(y, z) - \bar{u}_{\text{oct}}(y, z))^2 dy dz \right]^{1/2}, \quad (2.2)$$

where \bar{u}_{oct} denotes the mean velocity averaged over octants, as customarily reported by other authors. Parameters relevant for the statistical convergence of DNS are given in table 1. Following Vinuesa *et al.* (2016), in order to account for the effect of the streamwise length of the computational domain on statistical convergence, we consider effective time averaging intervals, $\Delta t_{av}^* = \Delta t_{av} L_x / (6h)$, expressed in eddy-turnover times, h/u_τ^* . For the sake of reference, previous studies used $\Delta t_{av}^* = 52h/u_\tau^*$ (Gavrilakis 1992), $\Delta t_{av}^* = 114h/u_\tau^*$ (Pinelli *et al.* 2010), $\Delta t_{av}^* = 112h/u_\tau^*$ (Vinuesa *et al.* 2014). The mean momentum balance convergence indicator is found to be less than 10^{-3} for all simulations, which is the convergence threshold suggested by Vinuesa *et al.* (2014). The symmetry indicator further suggests that distortions with respect to a eight-fold symmetric state are no larger than a few percent.

3. The secondary motions

A visual representation of the structure of the secondary motions is given in figure 2, where we show the computed mean streamwise vorticity ($\bar{\omega}_x = \partial \bar{v} / \partial z - \partial \bar{w} / \partial y$) and the corresponding stream function, evaluated by solving

$$\nabla^2 \psi = -\bar{\omega}_x. \quad (3.1)$$

As well established (Brundrett & Baines 1964) the time-averaged secondary motions consist of eight eddies having triangular shape, with obvious symmetry properties, whose main effect is to redistribute momentum excess from the channel core towards the duct corners, where momentum is less than the average because of the concurrent friction exerted by two walls. The outer scaling (u_b , h) used in the figure allows to draw the

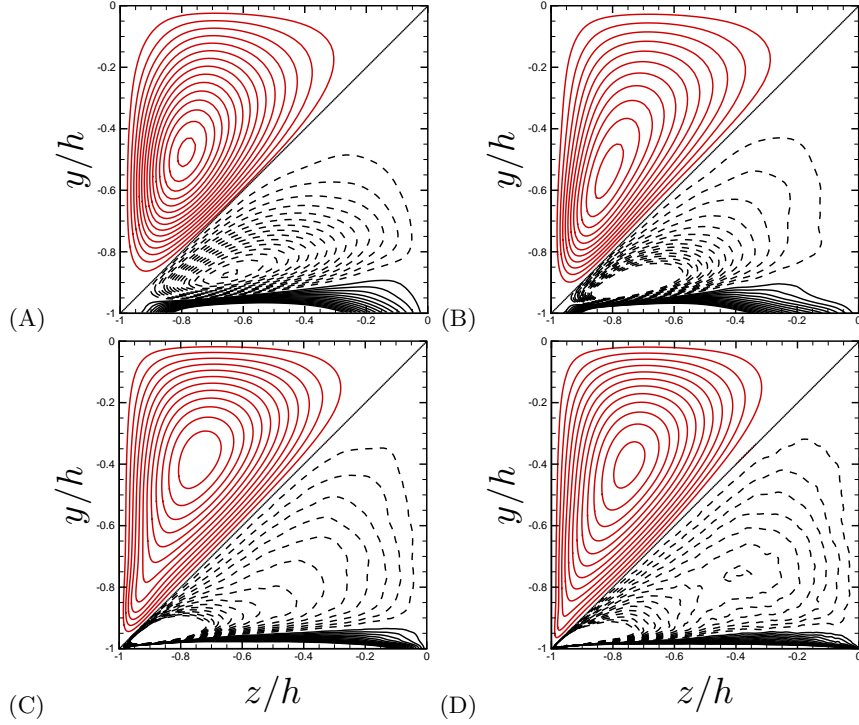


Figure 2: Vorticity contours (lower octant) and mean cross-flow streamlines (upper octant). Contours of $\bar{\omega}_x/(u_b/h)$ are shown from -0.24 to 0.24 , in intervals of 0.016 (dashed lines denote negative values), and contours of $\psi/(u_b h)$ are shown from 0 to 0.024 , in intervals of 0.0016 . Only one quadrant of the duct cross-section is shown. Refer to table 1 for nomenclature of the flow cases.

first conclusion that the intensity of the eddies is approximately unaffected by Reynolds number variations. Although the streamline topology is not changing, it appears that the geometry of the eddies does in fact change in two ways. First, the vortex centers exhibit a non-monotonic shift from the corners with the Reynolds number in a way to be discussed in detail later on, and second the streamlines penetrate deeper into the corners as Re increases. As also pointed out by Pinelli *et al.* (2010), the vorticity distribution is more complex than the streamline pattern. At low Reynolds number (A) a primary negative vorticity patch is observed in the duct core, which is accompanied by a mirror layer of positive vorticity signed near the wall, that forms as a result of the no-slip condition (Orlandi 1990). As the Reynolds number increases the main negative vorticity peak becomes stronger in amplitude, and it becomes progressively confined toward the duct corner, whereas the weaker core vorticity remains roughly of constant strength. A secondary negative vorticity peak eventually emerges, which is visible in (D) at about the same position as the centers of the cross-stream eddies. Hence, it appears that the strongest vorticity (hereafter referred to as corner vorticity) becomes progressively disconnected with the streamfunction distribution, whereas the core vorticity, which scales well in outer units (u_b/h), becomes closely associated with the streamfunction at high enough Re .

Deeper insight into the structure and scaling of the corner vorticity can be gained by using an inner representation, as in figure 3. As noted in previous studies, the highest

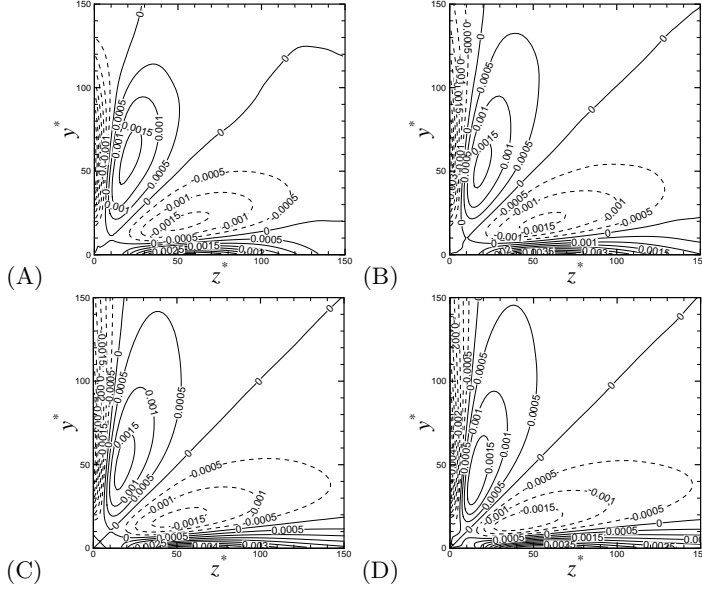


Figure 3: Streamwise vorticity contours near the bottom-left duct corner in inner coordinates, $z^* = (z + h)/\delta_v^*$, $y^* = (y + h)/\delta_v^*$. Contours are shown for $-0.004 \leq \omega_x/(u_b/\delta_v^*) \leq 0.004$, in intervals of 0.0005 (dashed lines denote negative values).

values of the vorticity tend to be concentrated about the corner bisector and at the wall. These motions are empirically found to scale well in mixed units (u_b, δ_v^*) , thus they become progressively confined to the duct corners as Re is increased, and their intensity increases when expressed in outer units, as was clear in figure 2. Despite its greater strength, this wall-confined vorticity does not contribute significantly to the secondary motions at high Re . This is easily understood, since the total circulation associated with the core vorticity is expected to scale as $u_b h$, whereas the contribution of the corner vorticity is expected to scale as $u_b \delta_v^*$, hence decreasing as Re_τ^* with respect to the former. This expectation is supported from the DNS data, which also shows that the ratio of the secondary (positive in figure 2) circulation and the primary (negative) circulation is about 0.42, regardless of the Reynolds numbers. A separate analysis (not reported here) further shows that the streamline pattern away from corners is not significantly altered in shape and intensity if the corner vorticity is cut off at the right-hand-side of equation (3.1).

Consistent with the previous observations, figure 4 shows that the velocity associated with the secondary motions well scales with u_b , with maximum intensity of about $2\%u_b$. Relative maxima are attained for the vertical velocity component along the corner bisector traced to the momentum inflow towards the duct corners, and parallel to the left sidewall and along the wall bisector as a consequence of the return motions to guarantee continuity. We may thus conclude that the correct scaling for the secondary flow is with outer units. The observed scaling of the corner vorticity can then be explained as a viscous effect, associated with retardation of the secondary stream scaling on $O(u_b)$, and occurring over a distance proportional to the viscous length scale δ_v^* , thus yielding the observed trend $\bar{\omega}_x \sim u_b u_\tau^*/\nu$. As an alternative one might assume that the relevant length scale in the duct corners is ν/u_b , which would then lead to $\bar{\omega}_x \sim u_b^2/\nu$. Based on the range of Reynolds number under scrutiny, the difference between the two trends is

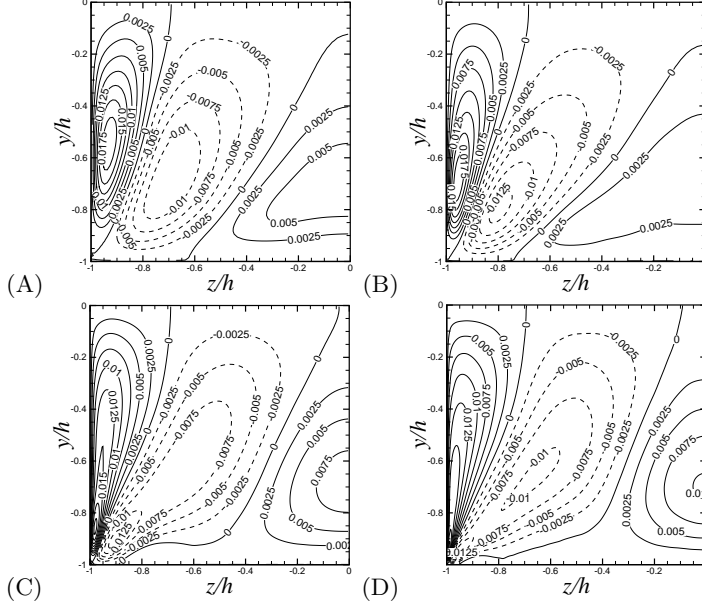


Figure 4: Contours of the mean cross-stream velocity component \bar{v} . Contour levels are shown for $-0.02 \leq \bar{v}/u_b \leq 0.02$, in intervals of 0.0025 (dashed lines denote negative values).

difficult to judge, however we are slightly in favour of the former option. Figure 4 also confirms that at sufficiently high Re a new maximum of v becomes isolated within the duct corners, which is associated with the corner vorticity. As clarified in figure 5, the intensity of these motions also scales with u_b , and it is geometrically similar (on a smaller scale though) to the core secondary flow. An interesting scenario thus emerges, which includes two concurrent contributions to the secondary motions: i) a core circulation, with typical velocity u_b and typical length scale h ; ii) a corner circulation with typical velocity still u_b and typical length scale likely to be δ_v^* . At low Reynolds number the two circulations basically coincide, whereas at higher Reynolds number the latter becomes progressively segregated to the duct corners, and the core circulation emerges.

Coming to the turbulent fluctuations, the distributions of the cross-stream turbulence intensity $\overline{v'^2}$ and of the cross-stream shear stress $\overline{v'w'}$ are shown in figures 6, 7. The turbulence intensity (figure 6) is found to scale reasonably well in magnitude with the mean friction velocity u_τ^* , especially at the higher Re . Near-wall peaks are observed associated with local production from mean shear, which approach the wall as the Reynolds number is increased. It should be noted that the intensity is higher at the left wall, with respect to which v' plays the role of cross-stream velocity fluctuation, whereas values are smaller at the bottom wall, where v' has the role of a wall-normal fluctuation. A ridge of $\overline{v'^2}$ is also observed along the corner bisector, which penetrates deeper into the corner as the primary peaks recede toward the wall. The secondary turbulent shear stress (figure 7) has comparatively much smaller values (by at least an order of magnitude), and it mainly develops along the corner bisector. Here again a two-scale organization is evident, whereby a relatively strong peak becomes segregated to the duct corner, and a weaker peak associated with the main secondary circulation emerges. In this case the scaling with u_τ^* is less clear than for $\overline{v'^2}$, although the peak values seem to level off at the higher Re .

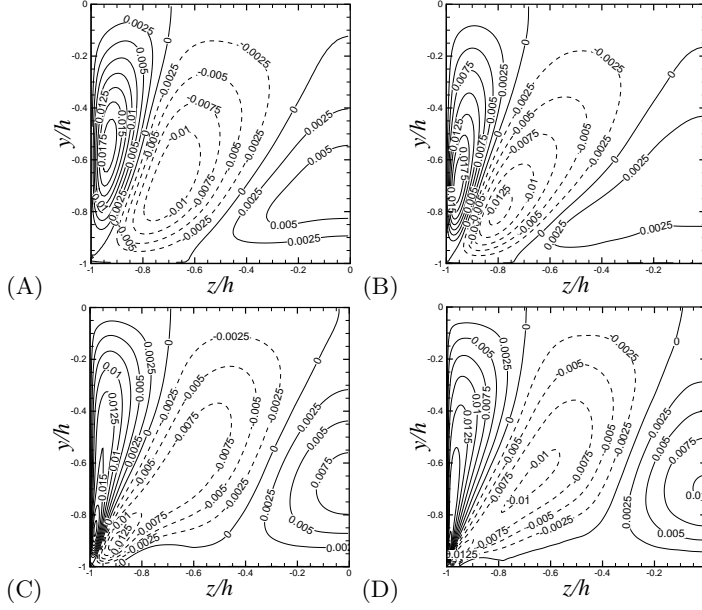


Figure 5: Contours of the mean cross-stream velocity component \bar{v} near the duct corner in inner coordinates, $z^* = (z + h)/\delta_v^*$, $y^* = (y + h)/\delta_v^*$. Contour levels are shown for $-0.02 \leq \bar{v}/u_b \leq 0.02$, in intervals of 0.0025 (dashed lines denote negative values).

Deeper insight into the nature of the secondary motions can be gained by inspecting the mean streamwise vorticity equation (Einstein & Li 1958)

$$\bar{v} \frac{\partial \bar{\omega}_x}{\partial y} + \bar{w} \frac{\partial \bar{\omega}_x}{\partial z} = \left(\frac{\partial^2}{\partial y^2} - \frac{\partial^2}{\partial z^2} \right) (-\overline{v'w'}) + \frac{\partial^2}{\partial y \partial z} (\overline{v'^2} - \overline{w'^2}) + \nu \left(\frac{\partial^2 \bar{\omega}_x}{\partial y^2} + \frac{\partial^2 \bar{\omega}_x}{\partial z^2} \right). \quad (3.2)$$

The various terms which appear in equation (3.2) are associated with the effect of mean cross-stream convection (left-hand side), secondary turbulent shear stress (first term at right hand side), normal stress anisotropy (second term), and viscous diffusion (third term). Their distributions as determined from DNS are shown in figure 8, where the two turbulence terms are merged together, and all terms are normalized with respect to $(u_b/\delta_v^*)^2$, which based on the previous discussion is the expected order of magnitude for the time derivative of $\bar{\omega}_x$. Also note that the distributions are only shown near the corners, where the various terms are sensibly different from zero. The figure indeed supports the alleged scaling of the various terms across the given Reynolds number range. Furthermore, it is indicative of a leading balance between the turbulence terms (which are regarded as production terms in the common interpretation) and viscous diffusion, whereas it appears that convection does not yield a significant contribution to the streamwise vorticity dynamics. This scenario is consistent with low- Re DNS studies (Gavrilakis 1992), but it contradicts the typical conclusions of experimental studies, which however are affected by significant uncertainties (Demuren & Rodi 1984).

More detailed information on the individual contribution of the anisotropy and the secondary shear stress terms is given in figure 9. It is found that the two terms are overall of the same order of magnitude, although the former is generally only considered in attempts of turbulence closure (Demuren & Rodi 1984). Detailed inspection of the figure shows that their spatial organization is similar, but they tend to be locally opposite in sign, with strong cancellation near the walls, where both terms assume individually very

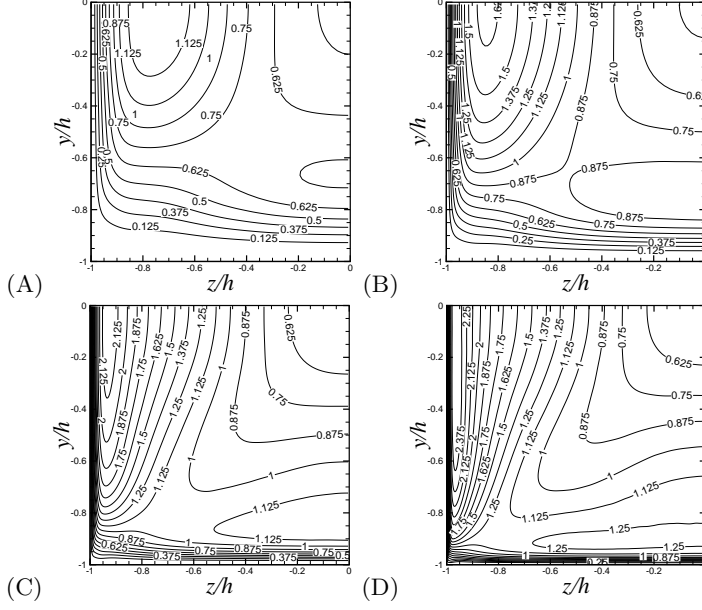


Figure 6: Contours of secondary turbulent normal stress, $0 \leq \overline{v'^2}/u_\tau^{*2} \leq 2$, in intervals of 0.125.

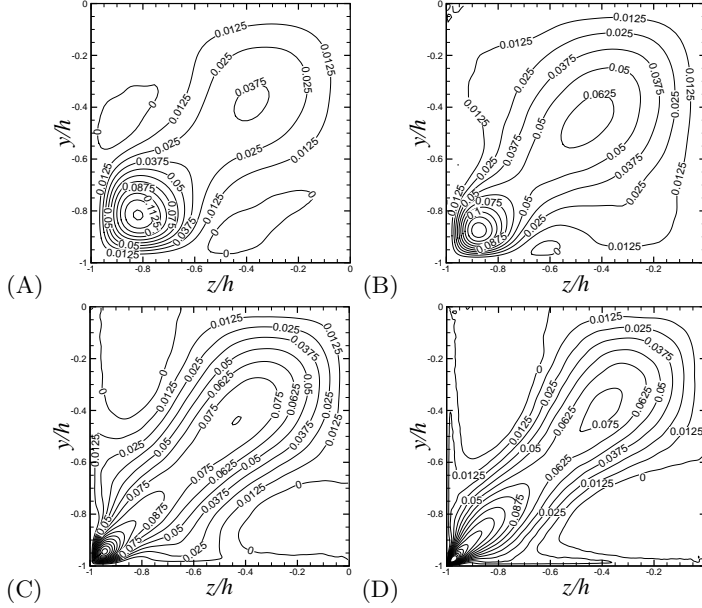


Figure 7: Contours of secondary turbulent shear stress, $0 \leq \overline{v'w'}/u_\tau^{*2} \leq 0.2$, in intervals of 0.0125.

large values. Comparing with their algebraic sum (repeated in panel (c) for convenience), it appears that non-zero values of turbulence production are primarily associated with large values of the secondary shear stress term.

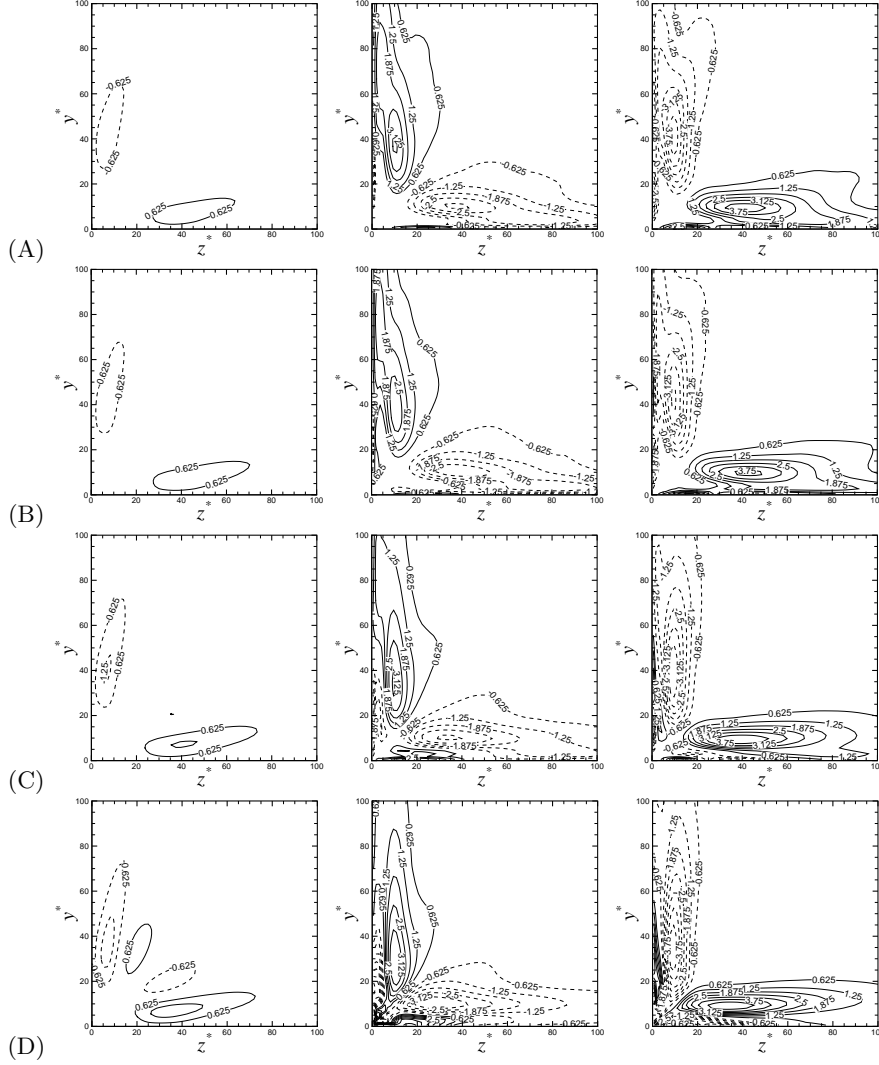


Figure 8: Terms in the mean streamwise vorticity budget equation (equation (3.2)) near the duct corners: mean convection (left column), turbulence (middle column), viscous diffusion (right column). Contour levels are shown for $-5 \leq (\cdot)/(u_b/\delta_v^*)^2 \cdot 10^6 \leq 5$, in intervals of 0.625 (dashed lines denote negative values).

4. Effect on the mean streamwise velocity field

A representation of the organization of the flow field in cross-stream traverses is provided in figure 10, where we show mean velocity vectors superposed to iso-contour lines of the mean streamwise velocity. Consistent with previous studies, we also observe the velocity contours to bulge toward the corners, under the action of the main secondary currents heading wall-ward along the corner bisector. On the other hand, the wall layer is found to thicken toward the wall bisector under the action of the return currents heading away from the wall. We find that the amount of distortion of the streamwise velocity iso-lines is non-monotonic with the Reynolds number, with minimum distortion observed for flow case B. This non-monotonic behavior is likely due to post-transitional effects, but based

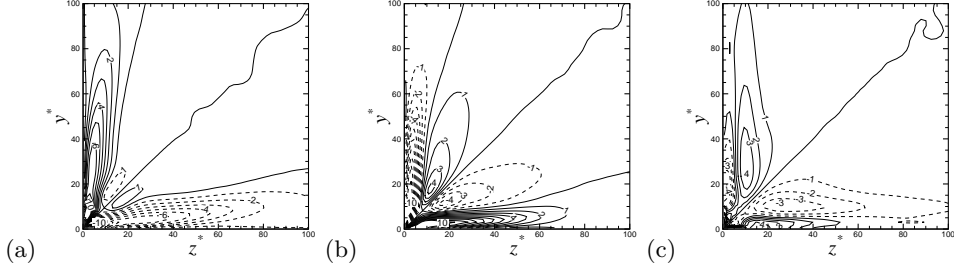


Figure 9: Turbulence terms in the mean streamwise vorticity budget equation (equation (3.2)) for flow case D: anisotropy term (a) secondary shear stress term (b), and their sum (c). Contour levels are shown for $-10 \leq (\cdot)/(u_b/\delta_v^*)^2 \cdot 10^6 \leq 10$, in intervals of 0.5 (dashed lines denote negative values).

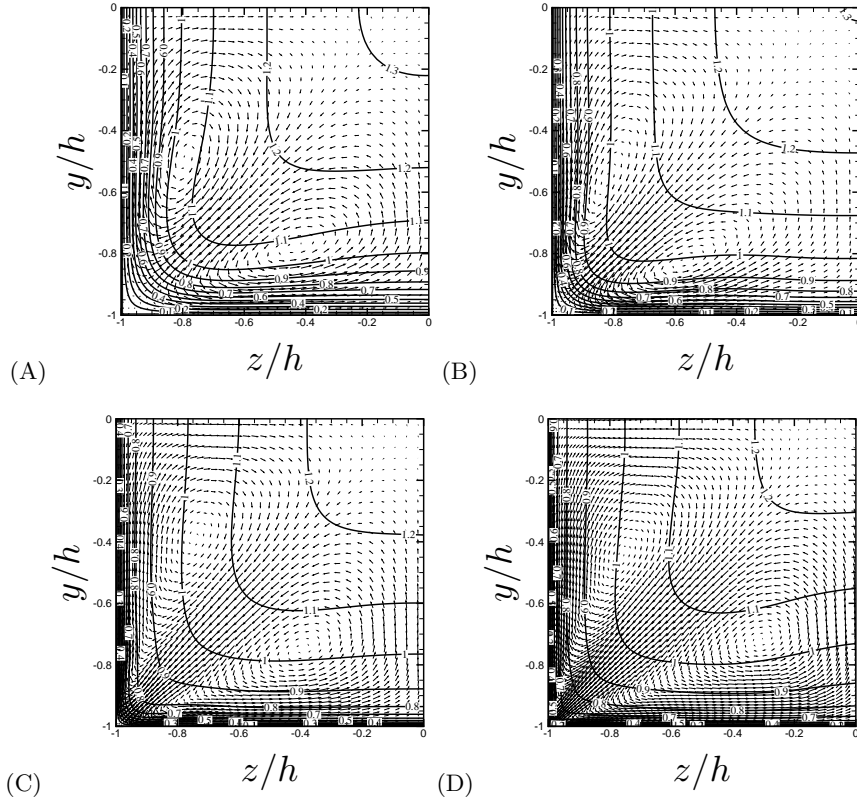


Figure 10: Mean streamwise velocity contours ($0 \leq \bar{u}/u_b \leq 1.3$) with superposed mean cross-stream vectors.

on the previous observation that the strength of the secondary motions is proportional to u_b , we expect distortions of \bar{u} to saturate at high enough Reynolds number.

The modulating effect of the secondary motions on the streamwise velocity field is made more evident from inspection of the local wall friction distribution, see figure 11. Rather than being uniform along the duct side, the local friction must obviously drop to zero towards the corners. A non-monotonic trend is also evident here, with maximum

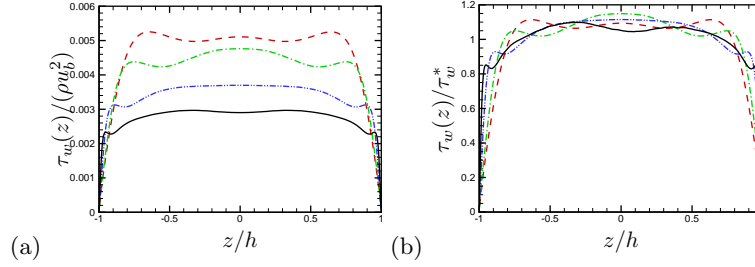


Figure 11: Local wall shear stress along the bottom wall, normalized with respect to the dynamic pressure (a), and with respect to its mean value (b) for flow case A (dashed), B (dash-dot), C (dash-dot-dot), D (solid).

values of the skin friction which are first attained midway between the corner and the wall bisector (flow case A), then at the wall bisector (flow cases B, C), and then again in between at higher Reynolds number. The behavior observed in flow case D is qualitatively very similar to what found in experimental measurements (Leutheusser 1984), generally carried out at higher Reynolds number, and it is consistent with the previously observed shape of the velocity iso-lines (see figure 10). In any case, disregarding the corner region, whose region of influence shrinks with Re , figure 11 shows that deviations of the local shear stress from its mean value are no larger than 10%.

Based on the previous observations, it is natural to study and compare the velocity statistics expressed in local wall units (+) and in global wall units (*). Figure 12 shows the mean velocity profiles as a function of the wall-normal distance up to the corner bisector (where mean velocity has a maximum), in local wall units. For reference purposes, the mean velocity profiles from DNS of pipe flow at approximately matching Re_τ are also reported (Wu & Moin 2008). Excellent collapse of the locally scaled profiles is recovered near the wall, also including the near-corner region. The distributions become more widespread past $y^+ \approx 10$, with maximum scatter of about $\pm 5\%$ in the “logarithmic” layer. When the mean friction velocity is used for normalization (see figure 13), scatter among the velocity profiles is observed near the wall as a result of the variation of the wall shear stress. Perhaps unexpectedly, this normalization does yield better collapse of the various curves further away from the wall, and near coincidence with the pipe velocity profiles, at least at high enough Re . This finding is probably related to the fact that mean momentum balance (as from equation (4.1)) is controlled by the imposed spatially uniform pressure gradient rather than by the nonuniform wall shear. Hence it is reasonable that, at least sufficiently away from walls, the flow should respond to the imposed pressure gradient rather than to the wall underneath. Inspection of figure 13 shows that transition from wall scaling to pressure scaling occurs at a wall distance of about $0.2h$, which is also the lower limit for the core region in canonical flows (Pope 2000). This interesting effect is impossible to observe in canonical wall-bounded flows, in which the wall shear stress is spatially uniform.

The inner-scaled distributions of the streamwise Reynolds stress are shown in figure 14. Along most of the wall, the behavior is qualitatively similar to canonical channel flow, with a near-wall peak of u' at $y^+ \approx 12$. The scatter among the various sections appears to be generally much larger than for the mean velocity field, although it probably becomes confined to the corner vicinity at high Re . An interesting feature is the behavior of the peak streamwise normal stress with the Reynolds number, which is larger at low Re and then levels off at increasing Re . This is apparently contradicting the increasing logarithmic trend of the wall-parallel velocity variances observed in canonical flows (Bernardini

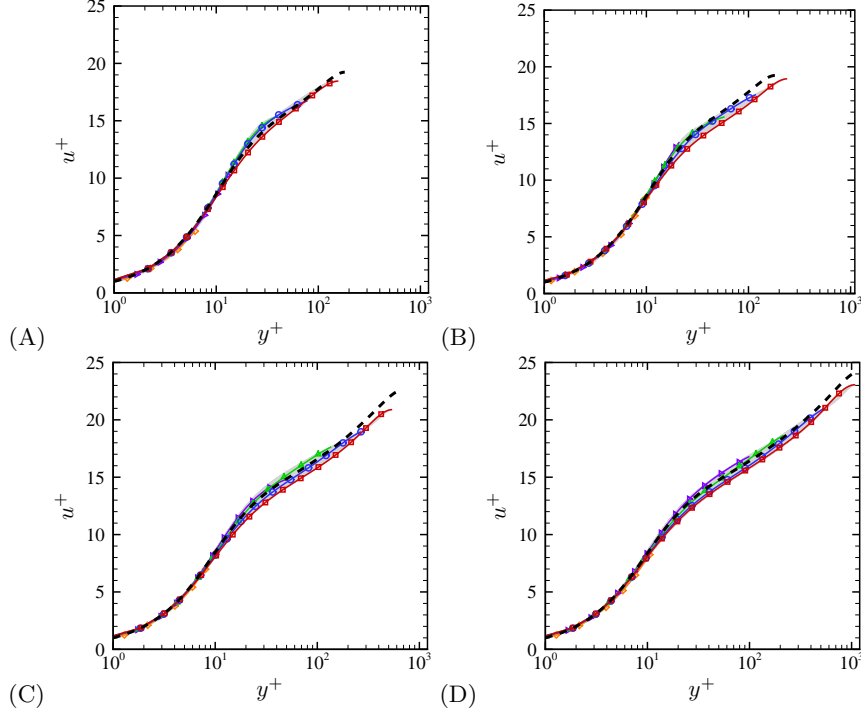


Figure 12: Mean streamwise velocity profiles along the y direction (up to the corner bisector), given in local wall units at all z . Representative stations along the bottom wall are highlighted, namely $z^* = 15$ (diamonds), $(z+h)/h = 0.1$ (right triangles), $(z+h)/h = 0.25$ (triangles), $(z+h)/h = 0.5$ (circles), $(z+h)/h = 1$ (squares). The dashed lines denote mean profiles from DNS of pipe flow at $Re_\tau = 181$ (A-B), $Re_\tau = 685$ (C), $Re_\tau = 1142$ (D), from Wu & Moin (2008).

et al. 2014), hence it would be interesting to carry out DNS at yet higher Reynolds number to verify whether the present observations are related to viscous effects, or whether mechanisms of inner-outer layer interactions in square ducts are different.

The terms in the budget of the mean streamwise momentum equation,

$$\bar{v} \frac{\partial \bar{u}}{\partial y} + \bar{w} \frac{\partial \bar{u}}{\partial z} = -\frac{\partial \overline{u'v'}}{\partial y} - \frac{\partial \overline{u'w'}}{\partial z} + \nu \left(\frac{\partial^2 \bar{u}}{\partial y^2} + \frac{\partial^2 \bar{u}}{\partial z^2} \right) - \bar{\Pi}. \quad (4.1)$$

are shown in figure 15. Here, the left-hand-side represents the contribution of convection from the secondary flows, and the terms at the right-hand-side represent the effects of Reynolds stress gradients and viscous diffusion, and the driving pressure gradient. Under global wall scaling (namely, each term is normalized with respect to u_τ^{*2}/δ_v^*), the magnitude of the various terms in the budget is approximately unaffected by Re variation. Away from corners, the leading balance is between the wall-normal turbulent shear stress gradients and viscous diffusion as in canonical flows, whereas mean cross-stream convection is at most one order of magnitude smaller. Convection appears to play a role near corners, where it is responsible for positive momentum transfer, and where it is balanced partly by diffusion and partly by locally negative turbulent stress gradient. Hence, this scenario corroborates the previous findings about the mean velocity profiles

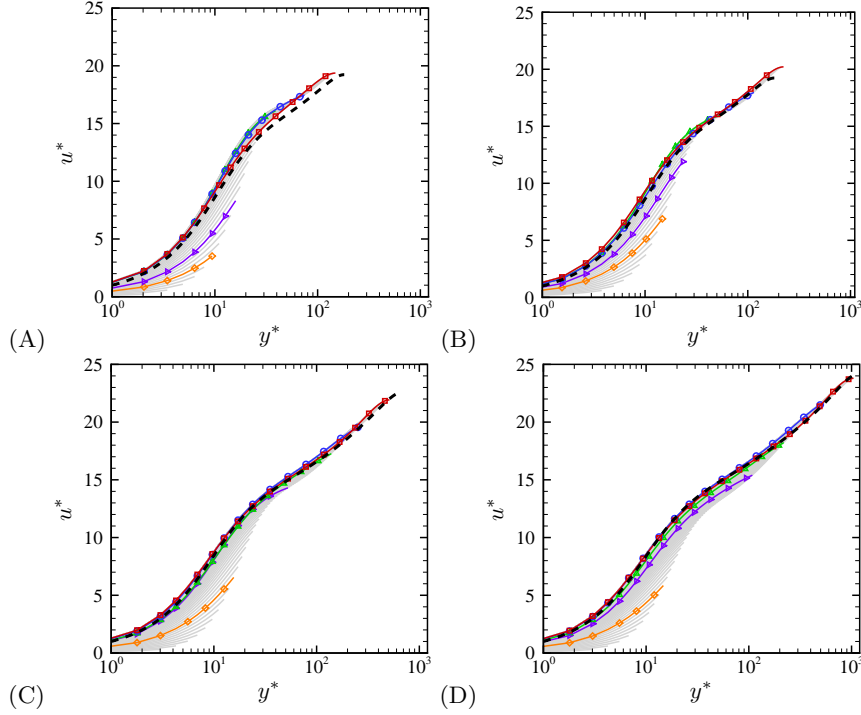


Figure 13: Mean streamwise velocity profiles along the y direction (up to the corner bisector), given in global wall units at all z . Representative stations along the bottom wall are highlighted, namely $z^* = 15$ (diamonds), $z/h = 0.1$ (right triangles), $z/h = 0.25$ (triangles), $z/h = 0.5$ (circles), $z/h = 1$ (squares). The dashed lines denote mean profiles from DNS of pipe flow at $Re_\tau = 181$ (A-B), $Re_\tau = 685$ (C), $Re_\tau = 1142$ (D), from Wu & Moin (2008).

(figures 12-13). Since convection has a minor effect, a logarithmic layer is expected to arise at sufficiently high Re , excepted in the close vicinity of corners.

The computed average friction factor, $f = 4C_f = 8\tau_w^*/(\rho u_b^2)$ is shown as a function of the bulk Reynolds number in figure 16, together with previous DNS data (Pinelli *et al.* 2010; Vinuesa *et al.* 2014), and assorted experimental data (Jones 1976). Overall, the agreement with other DNS is quite good, and results fall well within the scatter of the experimental data points. It is a common notion in the engineering practice (Schlichting 1979) that friction data for ducts with complex shape should collapse on the friction curves for canonical flows, provided the bulk Reynolds number is constructed using a suitable length scale, the most frequently used being the hydraulic diameter, defined as $D_h = 4A/P$, with A the cross-stream area and P the duct perimeter. Hence, $D_h = 2h$ for a square duct, and $Re_{D_h} = Re_b$. Several authors have noticed shortcomings of the hydraulic diameter concept, and proposed alternatives. For instance, Jones (1976) analyzed data for rectangular ducts, and come to the conclusion that a corrective factor should be applied to the conventional hydraulic diameter, which happens to be 1.125 for a square duct. More recently, Duan *et al.* (2012) proposed replacing the hydraulic diameter with the square-root of the cross-stream area. For the case of a square duct, this correction amounts to multiplying the bulk Reynolds number by a factor $2/\sqrt{\pi}$, not far from Jones' correction. For the sake of checking the validity of the above semi-empirical formulations,

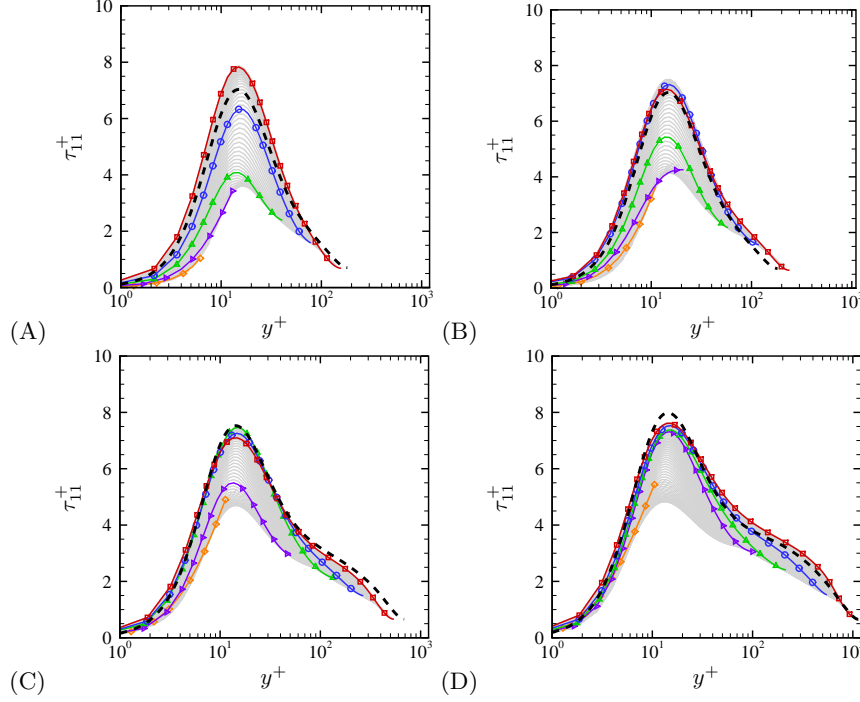


Figure 14: Mean streamwise turbulence intensity profiles along the y direction (up to the corner bisector), given in global local units at all z . Representative stations along the bottom wall are highlighted, namely $z^* = 15$ (diamonds), $z/h = 0.1$ (right triangles), $z/h = 0.25$ (triangles), $z/h = 0.5$ (circles), $z/h = 1$ (squares). The dashed lines denote mean profiles from DNS of pipe flow at $Re_\tau = 181$ (A-B), $Re_\tau = 685$ (C), $Re_\tau = 1142$ (D), from Wu & Moin (2008).

in figure 16 we also report numerical and experimental data for pipe flow (McKeon *et al.* 2004; Wu & Moin 2008), as well as the Karman-Prandtl theoretical friction law,

$$1/f^{1/2} = 2 \log_{10}(Re_{D_h} f^{1/2}) - 0.8. \quad (4.2)$$

Excellent agreement of the DNS data with equation (4.2) is observed using the standard hydraulic diameter formulation, especially for the higher- Re flow cases (C, D). However, proposed corrections to the hydraulic diameter scaling also seem to work very well (see the inset of figure 16), yielding perhaps better agreement at lower Reynolds number. The success of the hydraulic diameter concept (as well as its variations) may be tentatively explained based on the empirical finding (recalling figure 13(b)) that the inner-scaled mean velocity profiles along much of the duct perimeter exhibit near invariance in the outer layer also when scaled with global wall units. Hence, approximating the outer layer profiles with the classical log law, namely $u^* = 1/k \log y^* + C$, and integrating over an octant, the following expression for the bulk velocity results

$$\frac{u_b}{u_\tau^*} = \frac{Q}{4h^2 u_\tau^*} = 8 \int_0^h \int_0^z \left(\frac{1}{k} \log y/h + \frac{1}{k} \log Re_\tau^* + C \right) dy dz = \frac{1}{k} \log Re_\tau^* + C - \frac{3}{2k}. \quad (4.3)$$

The friction coefficient can then be evaluated as a function of Re_b from (4.3) using $C_f = 2(u_\tau^*/u_b)^2$, $Re_\tau^* = Re_b u_\tau^*/(2u_b)$. Equation (4.3) should be compared with the

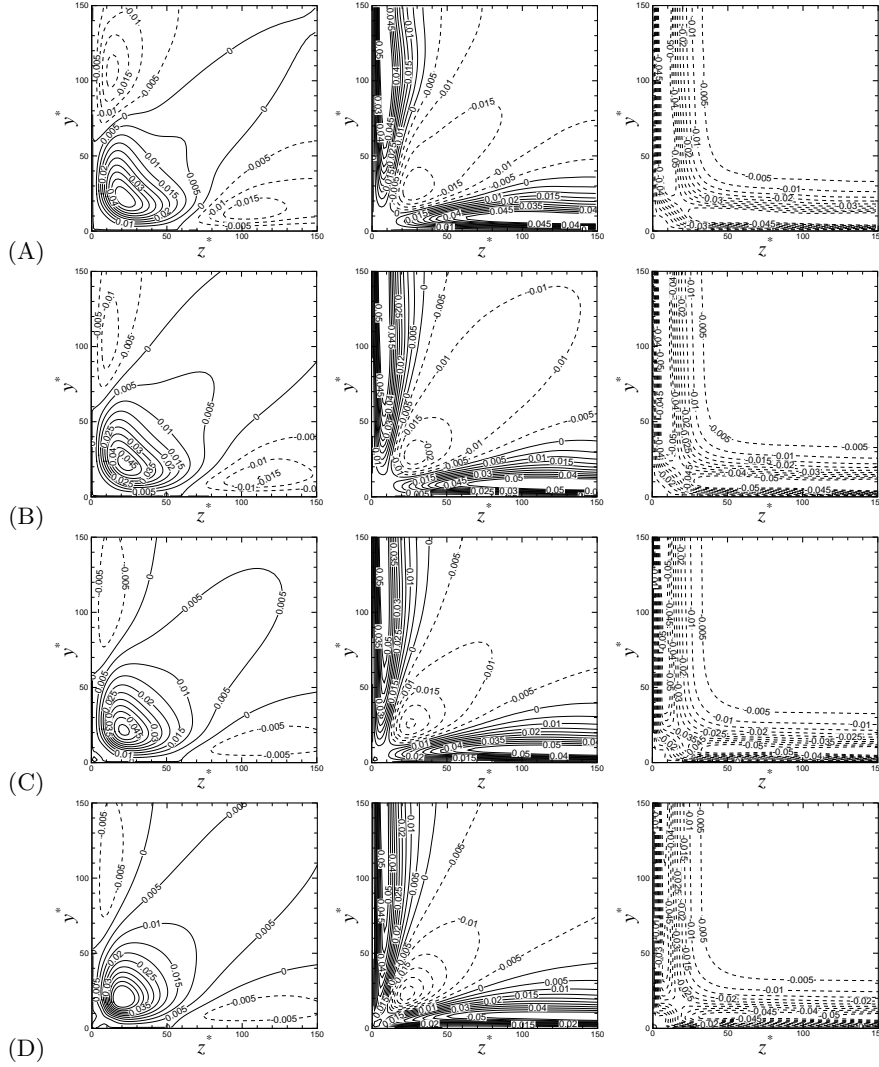


Figure 15: Terms in the mean streamwise momentum budget equation (4.1): convection (left column), turbulence (middle column), viscous diffusion (right column). Contour levels are shown for $-0.05 \leq (\cdot)/(u_\tau^{*2}/\delta_v^*)^2 \leq 0.05$, in intervals of 0.005 (dashed lines denote negative values).

corresponding expression for a circular duct

$$\frac{u_b}{u_\tau} = \frac{1}{k} \log Re_\tau + C - \frac{3}{2k}, \quad (4.4)$$

where $Re_\tau = Du_\tau/(2\nu)$, and leading to equation (4.2). The two expressions become identical provided $2h = D$, hence provided the Reynolds numbers based on the hydraulic diameter are the same. It is interesting that equation (4.3) is basically arrived at by neglecting the local wall shear stress variation along the duct perimeter, and disregarding the flow deceleration at corners. Apparently, these effects very nearly cancel out.

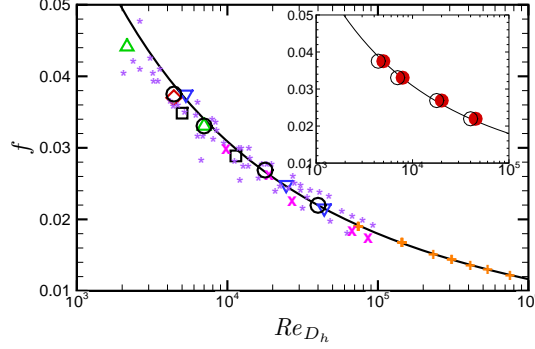


Figure 16: Friction factor ($f = 4C_f$) as a function of bulk Reynolds number based on the hydraulic diameter ($Re_{D_h} = u_b D_h / \nu$). Solid lines denote the reference friction curve for smooth pipe flow, equation (4.2). Symbols indicate present DNS data (circles), square duct DNS data of Pinelli *et al.* (2010) (diamonds) and Vinuesa *et al.* (2014) (squares), square duct experiments by Jones (1976) (stars) and Leutheusser (1963) (crosses), pipe flow DNS data of Wu & Moin (2008) (downtriangles), and pipe flow experiments by Mckeen *et al.* (2004) (plus symbols). The figure inset shows a comparison with the predictions of the square-root area law (Duan *et al.* 2012) (solid circles).

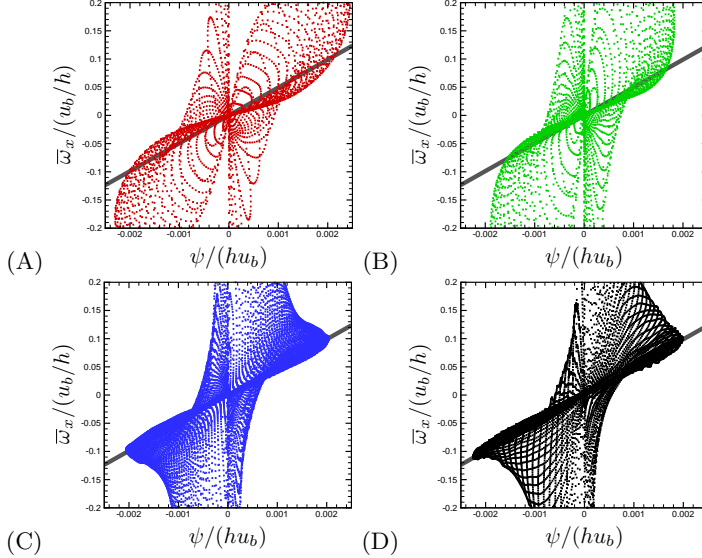


Figure 17: Scatter plots of cross-stream vorticity as a function of streamfunction. The diagonal line denotes the trend $\bar{\omega}_x = k^2 \psi$, with $k^2 = 49.452$.

5. A model for the secondary motions

Based on the outcome of the previous sections, it is possible to formulate a tentative model for the structure of the secondary motions. As shown in figure 8, the convective terms in the streamwise vorticity budget are negligible except in the corner proximity. Hence, the relevant condition for the existence of stationary cross-stream flow is $\bar{\omega}_x = f(\psi)$ (Batchelor 1969). This ansatz can be empirically verified based on the DNS data. Scatter plots of cross-stream vorticity and streamfunction are shown in figure 17, for

Mode	1	2	3	4	5	6	7	8	9	10
k^2	4.936	12.343	19.756	24.700	32.120	42.021	44.497	49.452	61.848	64.326

Table 2: List of ten smallest eigenvalues of Laplace operator in a $[-1 : 1] \times [-1 : 1]$ square.

all points in the channel cross-section. Despite the presence of significant dispersion, especially associated with near-wall points, the data suggest a tendency for ψ and $\bar{\omega}_x$ to become more and more correlated as Re is increased, as already pointed out commenting figure 2. Specifically, a nonlinear relationship is initially identified, which then yields a distinct linear variation at $Re_\tau^* \geq 500$. For flow case D, we find that over 70% of points in the duct cross-section is found within a band of $\pm 0.03u_b/h$ from the alleged linear relation. Based on this evidence, we argue that secondary motions at sufficiently high Re may be approximately characterized using equation (3.1) with the prescription $\bar{\omega}_x = k^2\psi$, which yields the classical Helmholtz equation for the cross-stream streamfunction,

$$(\nabla^2 + k^2)\psi = 0, \quad (5.1)$$

with $\psi = 0$ at the duct boundaries. Clearly, equation (5.1) cannot also accommodate the no-slip condition at the wall. However, we still expect that those solutions may be relevant in the high-Reynolds-number limit, also in light of the previously noticed evidence that viscous effects tend to be progressively confined to the near-wall region and to the duct corners. The cross-stream eddies would then correspond to eigenfunctions of equation (5.1), and the admissible values of the constant k^2 would be the corresponding eigenvalues. It is important that the steady equation for the streamfunction results from a time-evolving process which is controlled by turbulence production and viscous diffusion. Hence, it may be expected that in the long term, the only surviving mode(s) will be those which least damped from viscous diffusion, which occurs for those modes having smallest k^2 . The first few eigenvalues of (5.1) in a square domain are listed in table 2, some of them corresponding to multiple eigenfunctions. The DNS data (see figure 17) suggest that the mode which manifests itself is the one corresponding to the eighth smallest eigenvalue. Notably, this corresponds to the first eigenmode to respect the eight-fold statistical symmetry properties for square duct, and whose streamlines bisect the duct corners, hence respecting the physical requirement of being effective in transporting momentum from the bulk flow into the corner region. The Laplace eigenmode corresponding to $k^2 = 49.452$ is shown in figure 18(a). For the sake of comparison, in panel (c) we also show the streamlines obtained for flow case D after removing the near-wall vorticity, which is consistent with the assumptions under which the theory has been developed. Comparing figure 18(c) with the unfiltered streamfunction given in figure 2D shows that the main effect of removing the near-wall vorticity is to have greater penetration of the streamlines into the corners. The agreement of theory and filtered DNS field is apparently quite good.

It should be noted that a mathematical model for the secondary eddies in low-Reynolds number flow was also proposed by Wedin *et al.* (2008), based on the concept of self-sustained process (SSP). Based on that analysis, eigensolutions of the equation

$$(\nabla^4 + \lambda^2 \nabla^2)\psi = 0, \quad (5.2)$$

with homogeneous boundary conditions for ψ and its wall-normal derivative, should

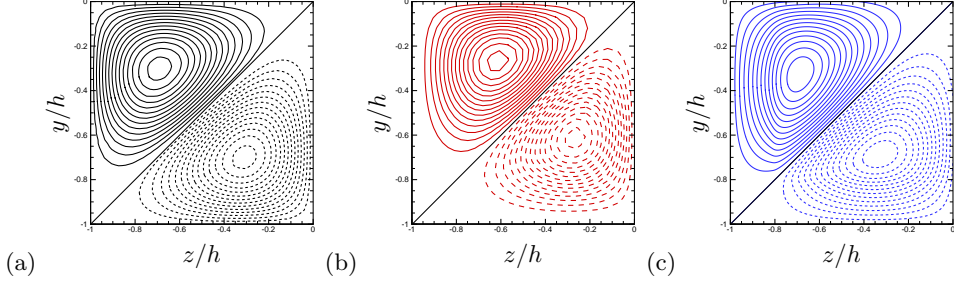


Figure 18: Eigenfunctions of equation (5.1) with $k^2 = 49.452$ (a), and of equation (5.2) with $\lambda^2 = 67.280$ (b). Panel (c) shows the streamlines for flow case D, upon removing the vorticity within a band of $200\delta_v^*$ from the walls.

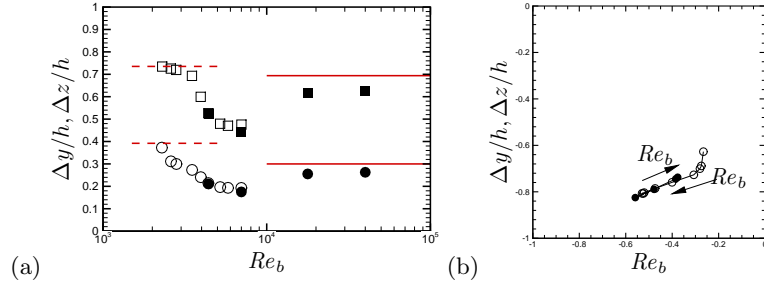


Figure 19: Position of vortex centers as a function of Reynolds number: (a) distance from bottom wall (circles) and from left wall (squares); (b) position in cross-stream plane. Solid symbols denote the present DNS data, open symbols denote DNS data of Pinelli *et al.* (2010). In panel (a) solid lines denote the vortex centers for eigensolutions of equation (5.1) with $k^2 = 49.452$, and dashed lines for eigensolutions of equation (5.2) with $k^2 = 67.280$.

emerge as a result of selective viscous decay. Specifically, eight eddies geometrically similar to those observed in developed flow were recovered for one particular eigenmode (corresponding to $\lambda^2 = 67.280$) whose shape is shown in figure 18(b). Although this eigenmode is not qualitatively too different from the filtered DNS field of panel (c) (but note that the values of ψ are here smaller near the walls as a consequence of the no-slip condition), the ψ - ω_x signature (not reported) highlights clustering of data points around the $\bar{\omega}_x = \lambda^2 \psi$ line, which is quantitatively different than observed in DNS (recalling figure 17).

More quantitative evaluation of the properties of the secondary eddies can be gained from figure 19, where we show the distance of the vortex centers from the duct walls as a function of the Reynolds number. Low-Reynolds-number data from Pinelli *et al.* (2010) are also shown. A non-monotonic drift of the vortex center position is found at low Reynolds number, whereby centers initially approach the corner, and then move away from it. Interestingly, it appears that the predictions of the SSP theory (Wedin *et al.* 2008) are in good agreement with DNS at low Re , whereas the Laplace eigenfunctions seem to yield the correct asymptotic trend at high Reynolds number.

6. Conclusions

We have carried out a DNS study of turbulent flow in a square duct in an unprecedentedly wide range of Reynolds numbers. The flow cases have been designed and carried out in such a way as to minimize possible uncertainties associated with limited grid resolution and/or lack of convergence of the statistical ensemble. In our opinion, this allows to draw more solid conclusions regarding the structure and the dynamical effect of the secondary motions than possible in previous studies. First, we find that the typical intensity of the secondary motions is very nearly unaffected by Reynolds number variation, scaling with the bulk velocity (in fact, a small fraction of it). Second, the secondary motions involve two coexisting circulations, with similar shape: i) a corner circulation, whose typical length scale is the global viscous length scale δ_v^* , and ii) a core circulation, whose typical length scale is h . Hence, the former is associated with higher values of the vorticity, but it becomes progressively confined to the duct corners as Re is increased. The core circulation on the other hand is weaker, but its effect is dominant over most of the duct cross-section. The DNS data show that mean cross-stream convection plays a minor role in the streamwise vorticity budget, which points to a simple structure of the secondary motions (at least away from walls), that involves a linear correlation between the averaged vorticity and the streamfunction, again well documented from DNS data at sufficiently high Reynolds number. A simple analytical characterization of the cross-stream eddies also directly arises under the assumption of negligible effect of mean convection, as of particular eigenmodes of the Laplace operator. Comparison with the shape of eddies in DNS shows a tendency for the latter to assume features similar to those theoretically predicted in the high- Re limit, whereas they resemble those predicted from viscous theories in the low- Re end. Of course, the intensity of the secondary flow is not predicted by the theory, being the likely result of a time-evolutionary process involving the competing effect of production from secondary stress gradients and viscous diffusion.

A quantitative characterization of the cross-stream eddies may be useful for certain purposes, such as for instance validating RANS turbulence models, and perhaps to develop predictive models for diffusion of inertial particles. However, regarding their direct effect on the bulk flow properties (mainly, friction), evidence reported in the present study seems to suggest that it is quite weak, if any. In first instance, analysis of the mean streamwise momentum equation shows that, with the exception of corners, cross-stream convection is much smaller than the turbulence terms and viscous diffusion. Hence, near-equilibrium layers do form adjacent to each wall, which exhibit very similar structure as the wall layers in canonical flows. Cross-stream convection has the main effect of modulating the thickness of those layers, hence yielding mild (10% at most) variation of the local wall friction along the duct perimeter. This effect probably further cancels out upon averaging over the duct perimeter, or (as is likely to be the case) because the flow away from walls responds to the imposed (spatially uniform) pressure gradient, rather than to the local wall friction. Furthermore, the effect of velocity distortions in corners is very small when integrated over the cross-section. As a result, it turns out that the mean velocity field can be characterized with good accuracy in terms of universal profiles normal to each wall and extending all the way to the duct corner bisector, with transition from wall scaling to pressure scaling occurring at a wall distance of $0.2h$. The resulting predictive formula for the friction coefficient (equation (4.3)) is identical to the theoretical friction formula for pipes, thus providing theoretical support for the concept of hydraulic diameter (and its variations) as a convenient way of incorporating the effect of the cross-stream geometry. For the case under scrutiny, refinements of the hydraulic diameter concept (Jones 1976; Duan *et al.* 2012) yield friction predictions with the same

accuracy as the baseline parametrization. Different geometries such as triangles, for which corrections are expected to be stronger, should be studied to identify the ‘best’ predictive formula.

It would be of extreme interest to carry over the results of the present study to yet higher Reynolds number, to further corroborate (or disprove) the findings. In any case, we find that the study of flows in duct with complex shapes, other than being interesting for its own sake, may also help to shed light onto phenomena of more canonical flows (e.g. pressure gradient or wall friction scaling), which cannot be conventionally sorted out.

We wish to thank Dr. D. Biau for providing the eigenmodes of equation (5.2), and Prof. A. Pinelli and Dr. R. Vinuesa for sharing their DNS data. We further acknowledge that most of the results reported in this paper have been achieved using the PRACE Research Infrastructure resource MARCONI based at CINECA, Casalecchio di Reno, Italy.

REFERENCES

- ADRIAN, R.J. & MARUSIC, I. 2012 Coherent structures in flow over hydraulic engineering surfaces. *J. Hydraulic Res.* **50**, 451–464.
- BATCHELOR, G. 1969 *An Introduction to Fluid Dynamics*. Cambridge University Press.
- BERNARDINI, M., PIROZZOLI, S. & ORLANDI, P. 2014 Velocity statistics in turbulent channel flow up to $Re_\tau = 4000$. *J. Fluid Mech.* **742**, 171–191.
- BRADSHAW, P. 1987 Turbulent secondary flows. *Annu. Rev. Fluid Mech.* **19**, 53–74.
- BRUNDRETT, E. & BAINES, W.D. 1964 The production and diffusion of vorticity in duct flow. *J. Fluid Mech.* **19** (03), 375–394.
- DEMUREN, A.O. & RODI, W. 1984 Calculation of turbulence-driven secondary motion in non-circular ducts. *J. Fluid Mech.* **140**, 189–222.
- DUAN, S., YOVANOVICH, M.M. & MUZYCHKA, Y.S. 2012 Pressure drop for fully developed turbulent flow in circular and noncircular ducts. *J. Fluids Eng.* **134** (6), 061201.
- EINSTEIN, H.A. & LI, H. 1958 Secondary currents in straight channels. *Trans. Am. Geophys. Union* **39** (6), 1085–1088.
- GAVRILAKIS, S. 1992 Numerical simulation of low-Reynolds-number turbulent flow through a straight square duct. *J. Fluid Mech.* **244**, 101–129.
- GEISSNER, F.B. & JONES, J.B. 1965 On some aspects of fully-developed turbulent flow in rectangular channels. *J. Fluid Mech.* **23** (04), 689–713.
- HOAGLAND, L.C. 1960 Fully developed turbulent flow in straight rectangular ducts – secondary flow, its cause and effect on the primary flow. PhD thesis, Department of Mechanical Engineering, Massachusetts Institute of Technology.
- HUSER, A. & BIRINGEN, S. 1993 Direct numerical simulation of turbulent flow in a square duct. *J. Fluid Mech.* **257**, 65–95.
- JONES, O.C. 1976 An improvement in the calculation of turbulent friction in rectangular ducts. *ASME J. Fluids Engng.* **98**, 173–181.
- KIM, J. & MOIN, P. 1985 Application of a fractional-step method to incompressible Navier-Stokes equations. *J. Comput. Phys.* **59**, 308–323.
- LAUNDER, B.E. & YING, W.M. 1972 Secondary flows in ducts of square cross-section. *J. Fluid Mech.* **54** (02), 289–295.
- LEUTHEUSSER, H.J. 1963 Turbulent flow in rectangular ducts. *J. Hydr. Div. ASCE* **89** (3), 1–19.
- LEUTHEUSSER, H. J. 1984 Velocity distribution and skin friction resistance in rectangular ducts. *J. Wind Eng. Ind. Aero.* **16**, 315–327.
- MANI, M., BABCOCK, D., WINKLER, C. & SPALART, P. 2013 Predictions of a supersonic turbulent flow in a square duct. In *51st AIAA Aerospace Sciences Meeting*, p. 860.
- MARIN, O., VINUESA, R., OBABKO, A.V. & SCHLATTER, P. 2016 Characterization of the secondary flow in hexagonal ducts. *Phys. Fluids* **28** (12), 125101.

- MCKEON, B.J., LI, J., JIANG, W., MORRISON, J.F. & SMITS, A.J. 2004 Further observations on the mean velocity distribution in fully developed pipe flow. *J. Fluid Mech.* **501**, 135–147.
- MODESTI, D. & PIROZZOLI, S. 2016a An efficient semi-implicit solver for direct numerical simulation of compressible flows at all speeds. *arXiv preprint arXiv:1608.08513* .
- MODESTI, D. & PIROZZOLI, S. 2016b Reynolds and Mach number effects in compressible turbulent channel flow. *Int. J. Heat Fluid Flow* **59**, 33–49.
- NEZU, I. 2005 Open-channel flow turbulence and its research prospect in the 21st century. *J. Hydraulic Eng.* **131**, 229–246.
- NIKURADSE, J. 1930 Turbulente strömung in nicht-kreisförmigen rohren. *Ing. Arch.* **1**, 306–332.
- OLIVER, T.A., MALAYA, N., ULERICH, R. & MOSER, R.D. 2014 Estimating uncertainties in statistics computed from direct numerical simulation. *Phys. Fluids* **26** (3), 035101.
- ORLANDI, P. 1990 Vortex dipole rebound from a wall. *Phys. Fluids* **2**, 1429–1436.
- ORLANDI, P. 2012 *Fluid flow phenomena: a numerical toolkit*, , vol. 55. Springer Science & Business Media.
- PINELLI, A., UHLMANN, M., SEKIMOTO, A. & KAWAHARA, G. 2010 Reynolds number dependence of mean flow structure in square duct turbulence. *J. Fluid Mech.* **644**, 107–122.
- PIROZZOLI, S. 2010 Generalized conservative approximations of split convective derivative operators. *J. Comput. Phys.* **229** (19), 7180–7190.
- PIROZZOLI, S. & BERNARDINI, M. 2013 Probing high-Reynolds-number effects in numerical boundary layers. *Phys. Fluids* **25**, 021704.
- POPE, S.B. 2000 *Turbulent flows*. Cambridge University Press.
- PRANDTL, L. 1927 Über die ausgebildete turbulenz. In *Verh. 2nd Int. Kong. für Tech. Mech.*.
- SCHLICHTING, H. 1979 Boundary layer theory. *McGraw-Hill, New York* .
- SPEZIALE, C.G. 1982 On turbulent secondary flows in pipes of noncircular cross-section. *Int. J. Eng. Sci.* **20** (7), 863–872.
- UHLMANN, M., PINELLI, A., KAWAHARA, G. & SEKIMOTO, A. 2007 Marginally turbulent flow in a square duct. *J. Fluid Mech.* **588**, 153–162.
- VINUESA, R., NOORANI, A., LOZANO-DURÁN, A., KHOURY, G.K.E., SCHLATTER, P., FISCHER, P.F. & NAGIB, H.M. 2014 Aspect ratio effects in turbulent duct flows studied through direct numerical simulation. *J. Turbulence* **15** (10), 677–706.
- VINUESA, R., PRUS, C., SCHLATTER, P. & NAGIB, H.M. 2016 Convergence of numerical simulations of turbulent wall-bounded flows and mean cross-flow structure of rectangular ducts. *Meccanica* **51** (12), 3025–3042.
- WEDIN, H., BIAU, D., BOTTARO, A. & NAGATA, M. 2008 Coherent flow states in a square duct. *Phys. Fluids* **20** (9), 094105.
- WU, X. & MOIN, P. 2008 A direct numerical simulation study on the mean velocity characteristics in turbulent pipe flow. *J. Fluid Mech.* **608**, 81–112.
- ZHANG, H., TRIAS, F.X., GOROBETS, A., TAN, Y. & OLIVA, A. 2015 Direct numerical simulation of a fully developed turbulent square duct flow up to $Re_\tau = 1200$. *Int. J. Heat Fluid Flow* **54**, 258–267.